

SUBMILLIMETER IMAGING OF THE LUMINOUS INFRARED GALAXY PAIR VV 114

D. T. FRAYER¹, R. J. IVISON², I. SMAIL³, M. S. YUN⁴, AND L. ARMUS⁵

Draft version September 23, 2018

ABSTRACT

We report on 450- and 850- μm observations of the interacting galaxy pair, VV 114 E + W (IC 1623), taken with the SCUBA camera on the James Clerk Maxwell Telescope, and near-infrared observations taken with UFTI on the UK Infrared Telescope. The system VV 114 is in an early stage of a gas-rich merger. We detect submillimeter (sub-mm) emission extended over $30''$ (12 kpc) and find a good correlation between the spatial distribution of the sub-mm and CO emission. Both the CO and sub-mm emission peak near the reddest region of VV 114 E and extend toward VV 114 W. The bulk of the sub-mm emission resides in the central region showing the largest CO velocity gradients, which is thought to mark the kinematic centroid of the merger remnant. We derived a total dust mass of $1.2 \times 10^8 M_{\odot}$, assuming a power-law distribution of dust temperatures. The sub-mm observations suggest that the majority of the dust is relatively cool ($T_{\text{d}} \sim 20\text{--}25\text{K}$), and the total dust mass is about 4 times higher than that inferred from the *IRAS* data alone. The system will likely evolve into a compact starburst similar to Arp 220.

Subject headings: galaxies: evolution — galaxies: individual (VV 114) — galaxies: interactions — galaxies: starburst

1. INTRODUCTION

Many extremely luminous infrared starbursts ($L_{\text{IR}} > 10^{11} L_{\odot}$) are merging systems, containing large reservoirs of molecular gas and dust (Sanders & Mirabel 1996, and references therein). To understand the evolution of the ISM and star formation in these systems, we require imaging observations of the molecular gas and dust reservoirs associated with the star-forming regions. Much of what is known about these systems has been inferred from interferometric CO observations (e.g., Scoville, Yun, & Bryant 1997; Downes & Solomon 1998). Our knowledge of the distribution of thermal dust emission in merging systems is lacking, due to the limited spatial resolution of the *Infrared Astronomical Satellite* (*IRAS*). With the commissioning of the new Sub-mm Common-User Bolometer Array (SCUBA, Holland et al. 1999) camera on the James Clerk Maxwell Telescope (JCMT), we can now directly image the thermal dust emission at relatively high ($\sim 8\text{--}15''$) spatial resolution.

The interacting galaxy pair VV 114 is only 80 Mpc away ($H_0 = 75 \text{ km s}^{-1} \text{ Mpc}^{-1}$) and is comprised of two stellar components separated by $15''$ (6 kpc in projection), designated VV 114 E and VV 114 W (Knop et al. 1994). The extreme infrared colors of VV 114 E indicate the presence of a large concentration of dust, while VV 114 W is relatively unobscured at optical wavelengths (Knop et al. 1994). The CO emission is distributed along a bar-like structure located in between the optical components (Yun, Scoville, & Knop 1994). The extended nature of the CO emission as well as the non-circular gas kinematics suggests that VV 114 is in an early stage of a gas-rich merger (Yun et al.

1994). The gas in VV 114 has already begun to flow into its central regions, while the stellar components are still well separated. This is consistent with theoretical models of young mergers (Barnes & Hernquist 1991, 1996).

In addition to the capability of SCUBA to resolve the VV 114 system, the sub-mm observations at 450 and 850 μm allow us to constrain the amount of cool material present ($T_{\text{d}} \lesssim 30\text{K}$). Preliminary evidence for the existence of cold dust in galaxies comes from the gas-to-dust ratios estimated using the warm dust masses derived from *IRAS*. The typical gas-to-dust ratios found for the bright *IRAS* galaxies are about an order of magnitude larger than the Galactic value derived from extinction studies, which includes dust at all temperatures (Devereux & Young 1990). A simple explanation for this discrepancy is that the majority of the dust in bright *IRAS* galaxies is cooler ($T_{\text{d}} \lesssim 30\text{K}$) than the warm material observed by *IRAS*. Observations with SCUBA can directly search for this component and provide a test of this hypothesis.

2. OBSERVATIONS

2.1. *Sub-mm Imaging*

Fully-sampled images of VV 114 were obtained using the SCUBA sub-mm camera during 1997 July and 1998 May. We used the 91-element short-wave array at 450 μm ($7''.8$ FWHM beam) and the 37-element long-wave array at 850 μm ($14''.7$ FWHM beam) during excellent conditions. Typical 850- μm zenith opacities were approximately 0.2, determined from hourly skydips. We obtained 7.7 ks of useful on-source integration time at 850 μm and 5.1 ks at 450 μm .

¹Astronomy Department, California Institute of Technology 105–24, Pasadena, CA 91125, USA

²Department of Physics and Astronomy, University College London, Gower Street, London, WC1E 6BT, UK

³Department of Physics, University of Durham, South Road, Durham, DH1 3LE, UK

⁴National Radio Astronomy Observatory, P.O. Box 0, Socorro, NM 87801, USA

⁵SIRTF Science Center, California Institute of Technology 100–22, Pasadena, CA 91125, USA

Fluxes were calibrated against Uranus and the flux densities determined for VV 114 at 450 and 850 μm are accurate to $\pm 18\%$ and $\pm 14\%$, respectively, including errors induced by opacity uncertainties and the absolute flux uncertainty of Uranus. The uncertainty in the 450 μm /850 μm flux ratio is approximately $\pm 7\%$, which represents the full dispersion in the measurements made on the separate nights. The error in the 450 μm /850 μm flux ratio is less than total uncertainty at either wavelength since the absolute flux calibration error of Uranus cancels for the ratio. Pointing was checked regularly using a nearby blazar. We estimate the overall positional accuracy of the submillimeter maps to be $\pm 2''$.

2.2. Near-infrared Imaging

Near-infrared, J - and K -band, imaging of VV 114 was obtained during the night of 1998 October 19 using the new UKIRT Fast-Track Imager (UFTI) on the 3.8-m UK Infrared Telescope (UKIRT) on Mauna Kea. UFTI comprises a 1024^2 Hg Cd Te HAWAII array cooled to 77 K and sensitive from 0.8 to 2.5 μm . The pixel scale is $0''.091$, allowing Nyquist sampling of the best seeing experienced on UKIRT, and the field of view is $92''$. The observations of VV 114 consisted of three sets of 9 exposures, two in K (2.2 μm) and one in J (1.2 μm), each of 30 s, dithered on a 3×3 grid with $9''.1$ spacing. These were interspersed by similar length observations of an offset sky region and dark exposures to allow the removal of the sky and instrumental backgrounds. The final stacked exposures represents 270 s in J and 540 s in K . The tip/tilt secondary on UKIRT was used to provide standard adaptive correction within our field, although the conditions were non-photometric and the seeing achieved was only mediocre, $\sim 0''.7$. Nevertheless, these images represent a substantial improvement in resolution over those presented by Knop et al. (1994).

3. RESULTS

Figures 1a & 1b show the 450- and 850- μm images of VV 114 taken with SCUBA. The integrated flux densities summed over the emission regions are 2.43 ± 0.44 Jy and 0.273 ± 0.038 Jy at 450 μm and 850 μm , respectively (Table 1). At 850 μm , we detect emission extended in the east-west direction, while at 450 μm we appear to resolve the central emission into two peaks (450 μm [1] and 450 μm [2] in Table 1). Given that the separation of the two 450 μm peaks is near the resolving limit of SCUBA, observations at higher resolution are required to confirm this double-peaked morphology. When the 450- μm data are convolved to the resolution of the 850- μm map, the data at both wavelengths show a similar shape, size, and position. At this resolution ($14''.7$), we fail to detect any significant variations in the $S(450\mu\text{m})/S(850\mu\text{m})$ flux ratio. Integrating over all emission regions, we find a flux ratio of 8.9 ± 0.6 , which is also the ratio measured for the peak of the sub-mm emission (at a resolution of $14''.7$). The consistencies in the 450- μm and 850- μm data would be expected if the bulk of the sub-mm emission is on the black-body tail of spectral energy distribution with dust temperatures $T \gtrsim 10$ K. Observations at higher resolution are required to search for possible variations in the $S(450\mu\text{m})/S(850\mu\text{m})$ ratio on smaller spatial scales.

The sub-mm emission lies along the CO bar-like structure (Fig. 1c), extending east-west between the two opti-

cal components. Both the CO and sub-mm emission peak near the brightest K -band source of VV 114 which is by far the reddest part of the VV 114 system, as indicated by the $J - K$ color map (Fig. 1d). Although the NIR data were not taken in photometric conditions, an approximate $J - K$ magnitude scale was derived by matching the data with the previously determined $J - K$ color of VV 114 W (Knop et al. 1994). The higher-resolution data presented here suggests a color of $(J - K) \simeq 3$ for the bright compact red component in VV 114 E. These results are consistent with those found for the Near-Infrared Camera and Multi-Object Spectrometer (NICMOS) data taken with the Hubble Space Telescope (Scoville et al. 1999).

4. DISCUSSION

4.1. Comparison of the Sub-mm Maps with Data at Other Wavelengths

The sub-mm, radio continuum, and CO emission from VV 114 all have roughly the same spatial extent. However, there are significant differences in their detailed structure. In particular, the radio sources (Condon et al. 1990; Condon et al. 1991) are located near the near-infrared (NIR) emission peaks (Knop et al. 1994), suggesting that these regions are responsible for the majority of the ongoing star formation. The sub-mm and CO peaks do not appear to be correlated with the radio and NIR peaks but tend to lie primarily in between VV 114 E + W.

The CO peak lies approximately $2''$ from the submillimeter peak, which is consistent within the positional uncertainties of the data sets. The general similarities of the CO and sub-mm maps suggest that both the CO(1 \rightarrow 0) and sub-mm emission probe the same material: the molecular gas and dust reservoir associated with the merger event. Despite these consistencies, there are differences in their detailed structure which may indicate optical depth or excitation effects in the CO emission. The CO emission is distributed more smoothly along the bar-like structure between VV 114 E and VV 114 W, while the sub-mm emission is more strongly peaked near VV 114 E. The tidal tails are also more apparent in the CO map, while the 450 μm emission is more extended in the east and south-west directions. The excess sub-mm emission in the east and south-west directions may be associated with HI tidal debris infalling into the central regions (Hibbard & Yun 1999).

VV 114 E is located near a peak of the sub-mm emission which is consistent with the high level of dust obscuration inferred from its extremely red NIR colors (Fig. 1d; also see Knop et al. 1994). VV 114 W, on the other hand, lies along a line of sight which is nearly free of sub-mm emission (Fig. 1a) and is consistent with the low level of extinction estimated at NIR wavelengths (Knop et al. 1994). The NIR data show that the star formation is occurring globally throughout the system, but the most active site is in the nucleus of VV 114 E, which is associated with the brightest radio sources in the 8.4-GHz sub-arcsec resolution map (Condon et al. 1991). The ISO 15- μm continuum also peaks strongly on the eastern nucleus of VV 114 (Yun et al. 1999). VV 114 E, itself, is comprised of two bright nuclear sources in the NIR (Knop et al. 1994). The northeast component of VV 114 E is strongest in J and is associated with the brightest compact radio source (marked by

a triangle symbol in Fig. 1) in the high-resolution radio map (Condon et al. 1991). The red south-west component of VV 114E is strongest in K (marked by a \times symbol in Fig. 1) and is associated with a region containing several bright, compact radio sources. This red south-west component of VV 114E is nearest to the position of the peaks in the sub-mm and CO emission, but is still offset by $3''.5$ – $5''$. This positional offset is larger than the positional errors in the data sets and hence may be significant.

Although most of the current star formation is occurring in and around the stellar components seen in the NIR (Knop et al. 1994), the central sub-mm and CO emission regions between the optical components may mark the location of a future major starburst given that these regions show the largest CO velocity gradients (Yun et al. 1994) and contain the bulk of the molecular gas and dust in the system. The apparent displacement of the sub-mm and CO emission from the most active regions of star-formation is consistent with the low HCN/CO ratio observed in VV 114 (Gao 1996). Typical infrared luminous galaxies show enhanced HCN/CO ratios, presumably due to the high density of the molecular gas in the starburst regions (Gao 1996). The low HCN/CO ratio in VV 114 may indicate that the bulk of the molecular gas is in regions of lower density and is displaced from the most active star-forming regions. Although the sub-mm emission of VV 114 is currently extended over 12 kpc, it is likely to evolve into a more compact starburst system similar to that seen for Arp 220 (Downes & Solomon 1998; Sakamoto et al. 1998). In the context of the numerical models for merging galaxies (Barnes & Hernquist 1996), VV 114 is an early-stage merger where the gas is accumulating within the central regions in advance of the stars. The system has yet to trigger a strong compact starburst at the dynamical centroid as seen for Arp 220 and other compact ultraluminous galaxies (Downes & Solomon 1998).

4.2. Estimating the Total Dust Mass

Observations at submillimeter wavelengths provide a better estimate of the total dust mass than that inferred from the *IRAS* data alone, since *IRAS* was not sensitive to cool dust. Assuming optically thin dust emission, the mass in dust is given by $M_d = S_\nu D^2 (k_d B[\nu, T_d])^{-1}$, where $B(\nu, T_d)$ is the black-body function for a frequency ν and a temperature T_d , D is the distance, and k_d is the dust absorption coefficient. We adopt $k_d = 10 \text{ g}^{-1} \text{ cm}^2 (\lambda/250\mu\text{m})^{-\beta}$, where $\beta = 1$ for $\lambda < 250\mu\text{m}$ (Hildebrand 1983). At longer wavelengths ($\lambda > 250\mu\text{m}$), the typical values for β range between 1 and 2. Empirically at long wavelengths, the Galactic cirrus is well fitted by $\beta \simeq 1.5$ (Masi et al. 1995), while Galactic star-forming regions have $\beta \simeq 2$ (Chini et al. 1986; Lis et al. 1998).

From the submillimeter measurements, we can directly estimate the value of β appropriate for VV 114 as a function of temperature. The integrated sub-mm flux density ratio is $S(450\mu\text{m})/S(850\mu\text{m}) = 8.9 \pm 0.6$. The value for β is calculated from $S(450\mu\text{m})/S(850\mu\text{m}) = (450/850)^{-\beta} \times B(666 \text{ GHz}, T_d)/B(353 \text{ GHz}, T_d)$. At $T_d = 20 \text{ K}$, the data imply $\beta = 2.15 \pm 0.11$. At the temperature of $T_d = 41 \text{ K}$ inferred from the *IRAS* data (Soifer et al. 1989), the sub-mm data imply $\beta = 1.76 \pm 0.11$. Since the mass-weighted average temperature of the dust is expected to be less than or equal to the *IRAS* dust temperature, the lower limit for

β in VV 114 is $\beta \geq 1.65$. In fact, we find (see below) that most of the dust is relatively cool in VV 114 ($T \simeq 20$ – 25 K) suggesting that $\beta \simeq 2$, which is similar to that observed for Galactic star-forming regions (Chini et al. 1986).

We fit thermal dust spectral energy distributions (SEDs) to the observational data in order to estimate the total dust mass in VV 114. Figure 2a shows models appropriate for a temperature of $T_d = 41 \pm 4 \text{ K}$ derived from the *IRAS* $60\mu\text{m}/100\mu\text{m}$ flux density ratio (Soifer et al. 1989). The dust mass inferred for this temperature is $(3 \pm 1) \times 10^7 M_\odot$ (Table 2). The uncertainty in k_d provides an additional uncertainty of about a factor of two in the dust mass. None of the single-component temperature models fit the sub-mm data. The low β models are inconsistent with the $S(450\mu\text{m})/S(850\mu\text{m})$ flux density ratio, and for $\beta \simeq 2$ the sub-mm fluxes are significantly higher than those expected from the *IRAS* data. A simple interpretation of the data is the presence of cooler material which was not detected by *IRAS*. Figure 2b shows a three-component fit to the data, assuming $\beta = 2$ at $\lambda > 250\mu\text{m}$. The mass of dust residing in the cool component ($T_d = 20 \text{ K}$) is 1 – $2 \times 10^8 M_\odot$, which is significantly larger than that found in the warm *IRAS* component ($T_d = 41 \text{ K}$, $0.3 \times 10^8 M_\odot$). By varying the allowed dust temperatures, the relative amount of dust in the warm (37–45 K) and cool (~ 15 – 25 K) components can be modified by factors of 2–3. The amount of dust in the hot component ($T_d = 150 \text{ K}$), constrained by the 12 and $25\mu\text{m}$ data, is negligible (Table 2).

More complicated models, which include several different grain types, cool cirrus, and warm starburst components could also be fitted to the data (Rowan-Robinson 1992; Andreani & Franceschini 1996). Although such models may be more realistic, the number of model parameters exceeds the number of observational data points for VV 114. For the model with three temperature components (Fig. 2b), there are six free parameters (mass and temperature of each component) for only six data points. In reality, there is likely to be a continuous range of dust temperatures.

A simple approach is to adopt a power-law distribution of dust temperatures; $dM_d/dT \propto T^{-x}$ (Xie, Goldsmith, & Zhou 1991). The total dust mass is determined by integrating the distribution function over a range of temperatures from T_{low} to T_{high} . The upper limit to the dust temperature has little effect on the total dust mass (e.g., de Muizon & Rouan 1985). We assume $T_{\text{high}} = 200 \text{ K}$. Fig. 2c shows dust SEDs computed for several different temperature distributions. Considering the small number of free parameters (x , T_{low} , and $M_d[\text{total}]$), the shape of the computed SEDs match the observational data remarkably well. The best fit to the 60–850 μm observational data occur for $T_{\text{low}} = 22$ and $x \simeq 6$. The 12–25 μm data are not fitted well with a single power-law distribution, but these data have little effect on the total dust mass. Since $M_d \propto T_d^{-5}$ for dust in thermal equilibrium (Soifer et al. 1989), we expect $x \simeq 6$. With this piece of theoretical insight, the SED is effectively fitted by only T_{low} and $M_d[\text{total}]$, after assuming an appropriate form for $k_d(\lambda)$. The best fit ($x = 6$; $T_{\text{low}} = 22 \text{ K}$) implies a total dust mass of $1.2 \times 10^8 M_\odot$. Assuming a power-law distribution of dust temperatures, the total dust mass is well constrained by the data. The error in fitting the dust mass is only about 25%. However,

considering the uncertainty in k_d at sub-mm wavelengths (Hughes, Dunlop, & Rawlings 1997), the derived dust mass is uncertain by approximately a factor of two.

4.3. Implications for Cool Dust in Luminous IRAS Galaxies

Most of the dust in VV 114 is at a temperature of $T_d = 20\text{--}25\text{ K}$. Based on the SCUBA data, the total dust mass derived for VV 114 is four times larger than that derived from the $60\text{--}100\mu\text{m}$ *IRAS* data. Since the *IRAS* colors for VV 114 are typical for its infrared luminosity (Soifer & Neugebauer 1991), we could expect to find similar results for other luminous *IRAS* sources. The existence of cool dust ($T_d < 30\text{ K}$) undetected by *IRAS* is not a surprising result. As stated in §1, the high gas-to-dust ratios in galaxies derived from the *IRAS* data of spiral galaxies imply the presence of cool material (Devereux & Young 1990). Millimeter observations of spiral galaxies also suggest massive cool dust reservoirs with $T_d \sim 10\text{--}20\text{ K}$ (Guélin et al. 1993, 1995; Franceschini & Andreani 1995). Recent SCUBA observations of NGC 891 support these results with the detection of a cool dust reservoir which is over an order of magnitude more massive than its warm dust component (Alton et al. 1998).

The results for VV 114 indicate that even very luminous *IRAS* galaxies can have cool dust reservoirs. Based solely on the *IRAS* data, the gas-to-dust ratio for VV 114 is $M(\text{H}_2)/M_d = 1100$ (Sanders, Scoville, & Soifer 1991), which is much higher than the Galactic value of about 100 (Devereux & Young 1990). By using the dust mass implied by the sub-mm data, we find a more realistic value of $M(\text{H}_2)/M_d \simeq 300$. These gas-to-dust ratios assume the Galactic CO to H_2 conversion factor. If the Galactic value is not applicable for ultraluminous galaxies (Solomon et al. 1997), then the gas-to-dust ratio for VV 114 could be reduced further by a factor of 2–4. Observations of other luminous *IRAS* galaxies will test the generality of these results.

The cool dust temperature for VV 114 may be related to its early-merger evolutionary phase. More evolved, luminous mergers have warm dust emission associated with a compact starburst and/or an active galactic nucleus (Mazzarella, Bothun, & Boroson 1991). For example, the sub-mm data for the evolved, compact starburst, Arp 220

(Rigopoulou, Lawrence, & Rowan-Robinson 1996), show no evidence for excess sub-mm emission associated with cool dust and can be fitted with a single-temperature, warm dust model of $T_d = 47\text{ K}$ (Klaas et al. 1997). The dust may be cooler in VV 114 because the majority of the dust is displaced from the star-forming regions traced by the NIR and radio emission peaks. Given the radio-to-FIR relationship (Helou, Soifer, & Rowan-Robinson 1985), we expect to find warm dust within the star-forming regions, especially near the most active region, VV 114 E. As VV 114 evolves into a compact gaseous system similar to Arp 220, the star formation is expected to increase in the central regions and the dust temperature should rise accordingly.

5. CONCLUSIONS

We present sub-mm maps of the young merger system VV 114. We detect sub-mm emission in excess of that expected from the *IRAS* data. This sub-mm excess suggests the presence of a cool, massive component of dust. By fitting a variety of dust models to the SED of VV 114, we derive a total dust mass of approximately $1 \times 10^8 M_\odot$, a temperature of $T_d \simeq 20\text{--}25\text{ K}$, and $\beta \simeq 2$. The majority of the dust is located in between the optical components, VV 114 E + W, near the suspected dynamical center of the merger remnant. The sub-mm emission regions correlate well with the CO emission regions, but do not correlate well with the peaks in the radio and NIR emission regions which are thought to trace the star-formation activity. The fact that the sub-mm emission is displaced from the most active regions of star formation may explain the cool temperature for the majority of the dust. Given the extremely large reservoir of gas and dust available in the central regions, VV 114 is expected to evolve into a more luminous central starburst, similar to that seen for Arp 220.

We thank the staff at the JCMT and UKIRT who have made these observations possible, and the Director of the JAC, Ian Robson, for the provision of discretionary time. DTF acknowledges support from NSF grant AST 96–13717 to the Owens Valley Millimeter Array; RJI and IRS acknowledge support from a PPARC Advanced Fellowship and a Royal Society Fellowship, respectively.

REFERENCES

- Alton, P. B., Bianchi, S., Rand, R. J., Xilouris, E., M., Davies, J. I., & Trewhella, M. 1998, *ApJ*, 507, L125
 Andreani, P., & Franceschini, A. 1996, *MNRAS*, 283, 85
 Barnes, J. E., & Hernquist, L. 1991, *ApJ*, 370, L65
 Barnes, J. E., & Hernquist, L. 1996, *ApJ*, 471, 115
 Chini, R., Kügel, E., & Kreysa, E. 1986, *A&A*, 167, 315
 Condon, J. J., Helou, G., Sanders, D. B., & Soifer, B. T. 1990, *ApJS*, 73, 359
 Condon, J. J., Huang, Z.-P., Yin, Q. F., & Thuan, T. X. 1991, *ApJ*, 378, 65
 de Muizon, M., & Rouan, D. 1985, *A&A*, 143, 160
 Devereux, N. A., & Young, J. S. 1990, *ApJ*, 359, 42
 Downes, D., & Solomon, P. M. 1998, *ApJ*, 507, 615
 Franceschini, A., & Andreani, P. 1995, *ApJ*, 440, L5
 Gao, Y. 1996, Ph.D. Thesis, State University of New York at Stony Brook
 Guélin, M., Zylka, R., Mezger, P. G., Haslam, C. G. T., & Kreysa, E. 1995, *A&A*, 298, L29
 Guélin, M., Zylka, R., Mezger, P. G., Haslam, C. G. T., Kreysa, E., Lemke, R., & Sievers, A. W. 1993, *A&A*, 279, L37
 Helou, G., Soifer, B. T., & Rowan-Robinson, M. 1985, *ApJ*, 298, L7
 Hibbard, J. E., & Yun, M. S. 1999, in preparation
 Hildebrand, R. H. 1983, *QJRAS*, 24, 267
 Holland, W. S., et al., 1999, *MNRAS*, in press (astro-ph/9809122)
 Hughes, D. H., Dunlop, J. S., & Rawlings, S. 1997, *MNRAS*, 289, 766
 Klaas, U., Haas, M., Heinrichsen, I., & Schulz, B. 1997, *A&A*, 325, L21
 Knop, R. A., Soifer, B. T., Graham, J. R., Matthews, K., Sanders, D. B., & Scoville, N. Z. 1994, *AJ*, 107, 920
 Lis, D. C., Serabyn, E., Keene, J., Dowell, C. D., Benford, D. J., Phillips, T. G., Hunter, T. R., & Wang, N. 1998, *ApJ*, 509, 299
 Masi, S., et al. 1995, *ApJ*, 452, 253
 Mazzarella, J. M., Bothun, G. D., & Boroson, T. A. 1991, *AJ*, 101, 2034
 Rigopoulou, D., Lawrence, A., & Rowan-Robinson, M. 1996, *MNRAS*, 278, 1049
 Rowan-Robinson, M. 1992, *MNRAS*, 258, 787
 Sakamoto, K., Scoville, N. Z., Yun, M. S., Crosas, M., Genzel, R., & Tacconi, L. J. 1999, *ApJ*, in press (astro-ph/9810325)
 Sanders, D. B., & Mirabel, I. F. 1996, *ARA&A*, 34, 749
 Sanders, D. B., Scoville, N. Z., & Soifer, B. T. 1991, *ApJ*, 370, 158
 Scoville, N. Z., et al. 1999, in preparation
 Scoville, N. Z., Yun, M. S., Bryant, P. M. 1997, *ApJ*, 484, 702

Soifer, B. T., Boehmer, L., Neugebauer, G., & Sanders, D. B. 1989, AJ, 98, 766
 Soifer, B. T., & Neugebauer, G. 1991, AJ, 101, 354
 Solomon, P. M., Downes, D., Radford, S. J. E., & Barrett, J. W. 1997, ApJ, 478, 144

Xie, T., Goldsmith, P. F., & Zhou, W. 1991, ApJ, 371, L81
 Yun, M. S., et al. 1999, in preparation
 Yun, M. S., Scoville, N. Z., & Knop, R. A. 1994, ApJ, 430, L109

FIG. 1.— SCUBA (a) 450- μm and (b) 850- μm maps. The 1σ rms levels are 75 and 4.4 mJy beam $^{-1}$ for the 450- and 850 μm data, respectively. Contour levels are plotted at $\sigma \times (-2, 2, 3, 4, 5, 6, 8, 10, 12)$ for the 450- μm map and $\sigma \times (3, 4, 5, 6, 8, 10, 12, 15, 20, 25, 30, 35)$ for the 850- μm map. The 2 μm NIR peaks, signifying the positions of VV 114 E + W are shown by the \times and $+$ symbols (Knop et al. 1994). The 8.4-GHz radio peak is shown by the \triangle symbol (Condon et al. 1991) and the \diamond symbols show peaks in the optical R -band emission (Knop et al. 1994). Panel (c) shows the integrated CO(1 \rightarrow 0) emission (Yun et al. 1994). Contour levels are plotted at 1 Jy km s $^{-1}$ beam $^{-1} \times (5, 10, 15, 30, 50, 70)$. For panels (a), (b), and (c) the beam sizes are shown in the lower left of each panel. Panel (d) shows the NIR ($J - K$) color map, where lighter pixels indicate redder colors and darker pixels represent bluer colors. The color map ranges from $(J - K) = 0.9$ for the blue regions of VV 114 W to the very red compact region in VV 114 E which has a color of $(J - K) = 3.0$ at the observed resolution ($0''.7$).

FIG. 2.— Model fits to the spectral energy distribution of VV 114. The *IRAS* data points are from Soifer et al. (1989). Panel (a) shows single temperature models ($T_d = 41$ K) based on the *IRAS* 60–100 μm data for $\beta = 1, 1.5$ (dotted lines), and $\beta = 2$ (solid line). No single temperature model can fit the data. Panel (b) shows a three-component model fit to the data, assuming $\beta = 2$ for $\lambda > 250\mu\text{m}$. The three different components are plotted as dotted lines, and their sum is shown by the solid line. Panel (c) shows models based on a distribution of dust temperatures; $dM_d/dT \propto T^{-x}$ (see §4.2). The solid line represents the best model fit with $T_{\text{low}} = 22$ K and $x = 6$. The dotted lines show models with different values of x , while the dashed lines show fits based on different values of T_{low} .

TABLE 1
SUBMILLIMETER OBSERVATIONAL RESULTS

Parameter		450 μ m[1]	450 μ m[2]	850 μ m
α (J2000) ^{a,b}	01 ^h 07 ^m	47 ^s .55	47 ^s .15	47 ^s .35
δ (J2000) ^{a,b}	-17 ^o 30'	28''9	26''1	27''2
Beam (FWHM)		7''8		14''7
Flux (Jy) ^c		2.43 \pm 0.44		0.273 \pm 0.038

^aPositional uncertainty is $\pm 2''0$.

^bDerived from a Gaussian fit to the peak.

^cTotal integrated flux.

TABLE 2
DUST MODELS

Model	Fitted Data	T_d (K)	M_d ($10^7 M_\odot$)	Notes
Single Component	60–100 μ m	41	3.0	Fig. 2a
Three Component	12–850 μ m	20	13	Fig. 2b
		41	2.7	Fig. 2b
		150	0.0018	Fig. 2b
Temperature Distribution	450–850 μ m	15	21	$T_d = T_{low}$, $x = 6$, Fig. 2c
	450–850 μ m	30	8	$T_d = T_{low}$, $x = 6$, Fig. 2c
	60–850 μ m	22	12	$T_d = T_{low}$, $x = 6$, Fig. 2c

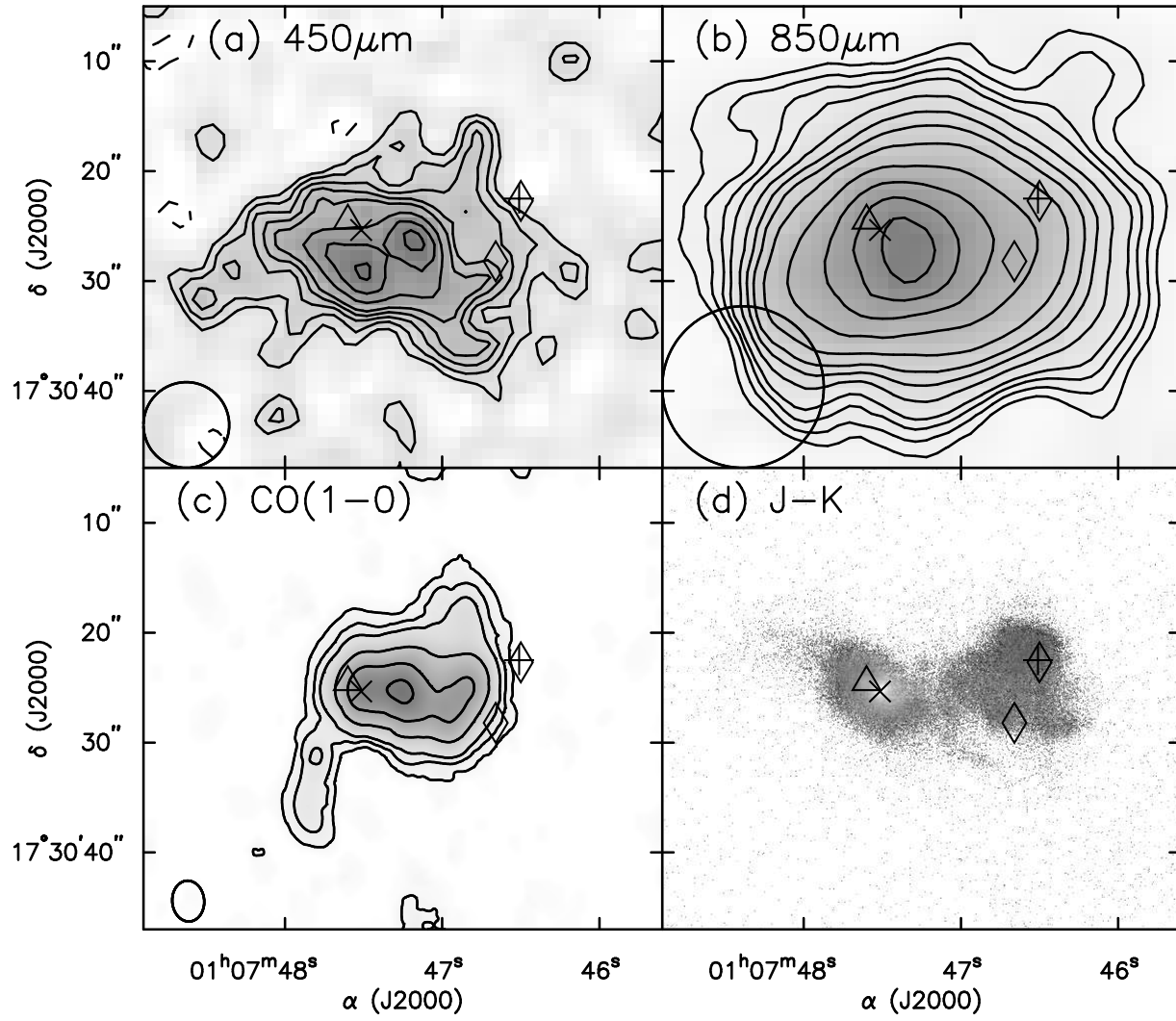


FIG. 1.—

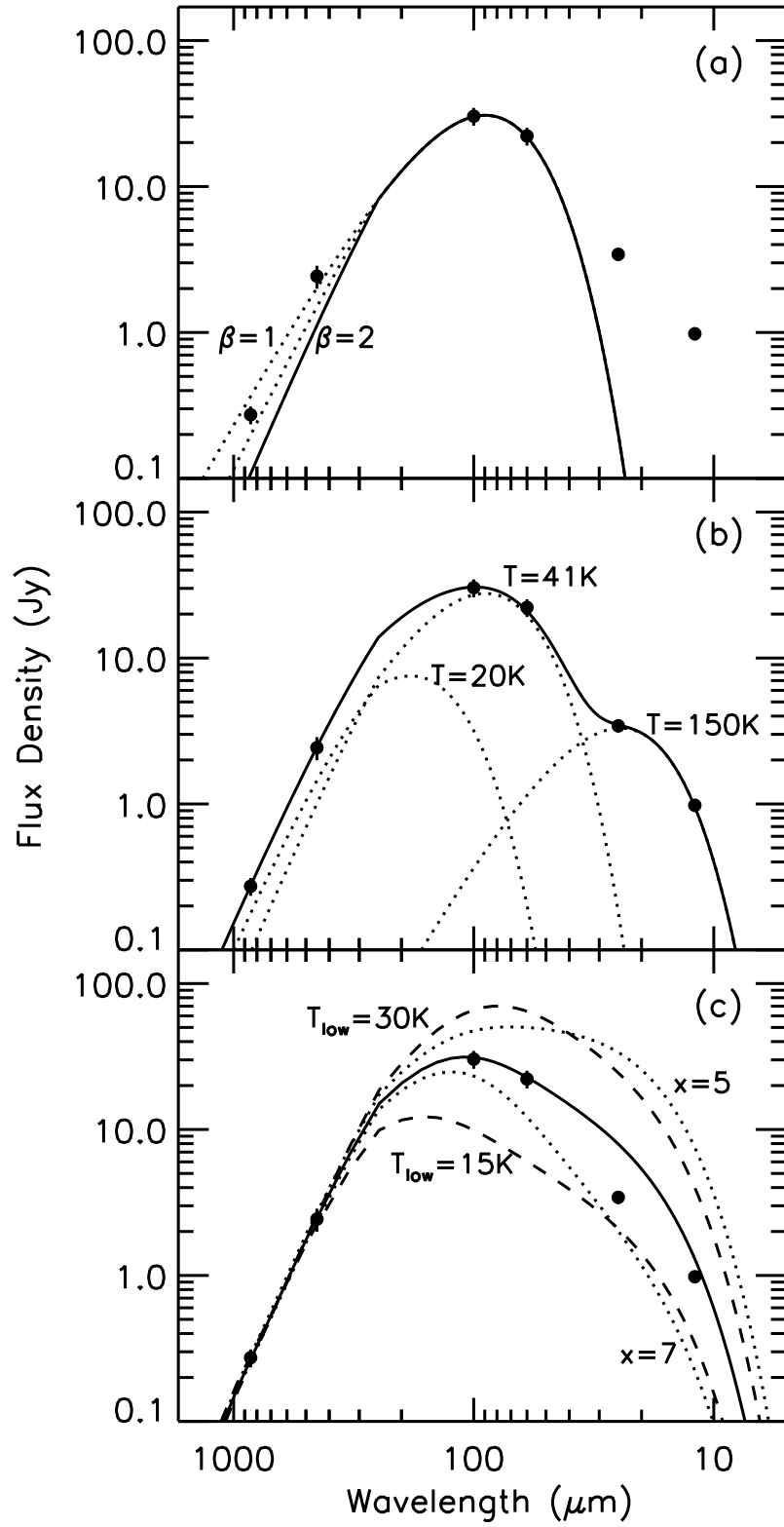


FIG. 2.—

